

# KINETIC CHARACTERIZATION OF LOW-VELOCITY POSITIVE COLLISION OF DOUBLE DROPLETS

*Zhiheng MA, Jinjuan SUN\*, Jianhui TIAN, Jinxiu Qu*

School of Mechatronics Engineering, Xi'an University of Technology, Xi'an 710021, China. \*Corresponding author; Email address: [sunjinjuan@xatu.edu.cn](mailto:sunjinjuan@xatu.edu.cn)

*Droplet positive collision is a complex process involving heat transfer in gas-liquid-solid three-phase flow and droplet collide dynamics. In order to study the kinetic behavior of droplets under positive collision in low velocity ( $v < 2$  m/s), this paper focuses on the spreading, vibration and fracture characteristics of double droplets by numerical simulation. First, the accuracy of the model is verified by experimental comparison. The effects of droplet diameters, collision velocities and wall contact angles on the spreading process are analyzed, and the spreading factor curves are plotted. Then, the droplet rebound vibration after collision fusion is equated to a single-degree-of-freedom damped vibration system, and the peak vibration height variation curve of the fused droplet is obtained by nonlinear fitting. Considering the droplet phase change, the influence law of different conditions on the vibration damping factor and vibration time of the fused droplet is studied. Finally, it is found that rebound fracture and spreading fracture occur after the fusion of double droplets under positive collision, and the critical values of collide velocity required for the occurrence of the above phenomenon are found. To provide a reliable theoretical basis for the study of heat and mass transfer processes after multiple droplets collide the wall.*

*Key words: Double droplets positive collide; Decay vibration; Kinetic properties; Damping coefficients; Vibration time; Fracture*

## 1. Introduction

The positive collision phenomenon of double droplets is widely found in aerospace, industrial and agricultural applications [1]. For example, the collide phenomenon of fuel droplets on the combustion chamber walls, wing icing phenomenon, 3D printing, inkjet printing, spray cooling, spraying, pesticide spraying, etc. Droplet spreading, vibration, and fracture kinetic behaviors are formed after positive collision of double droplets [2-7], which can complicate the droplet icing mechanism on the cold wall surface if the wall temperature is too low. Therefore, it is of great interest to investigate the mechanism of the kinetic characteristics of double droplets under positive collision.

In recent years, the kinetic properties of single and double droplets have been intensively studied by many scholars. Fujimoto et al. [8-9] conducted an experimental study of double droplets continuously colliding a solid wall and investigated the effects of the size, spacing, collide velocity, wall temperature, and wall contact angle of the double droplets on the spreading process. Yuvaraj et al. [10] found experimentally that the smaller the wall contact angle, the larger the contact area of the droplets, which increases the heat transfer coefficient and condensation rate. Lin et al. [11] found that a single

droplet striking a hydrophilic wall would have a longer motion wave resulting in more energy dissipation during the oscillation. Manglik et al. [12-13] equated the vibration of a single droplet to a spring-damped system, used a triangular fitting function to describe the droplet height variation, gave the damped vibration equation, and verified the droplet oscillation period theory of Fedorchenko [14]. Sharp et al. [15] used surface wave theory and optimized the Sharp and Landau droplet model to obtain a model of the vibration of droplet lagging behind at low velocity simultaneously.

In this paper, firstly, the experimental platform is built to conduct double droplets positive collide experiments, and the accuracy of the model is verified by comparing with the simulation results. Then, the effects of different droplet diameters, collide velocities and wall contact angles on the spreading process of double droplets positive collision are investigated, and the spreading factor curves are plotted. Next, the peak variation curve of droplet vibration height after fusion is obtained by nonlinear fitting, and the influence law of different collide velocity, wall temperature and wall contact angle on vibration damping factor and vibration time is studied. Finally, rebound fracture and spreading fracture phenomena may occur after the positive collision fusion of double droplets. The reasons for the occurrence of both fracture phenomena are analyzed, and the critical collide velocity curves required for the occurrence of fracture phenomena are plotted.

## 2. Model and method

Figure 1 shows a schematic diagram of a double droplets low-velocity positive collision. As shown in the figure, droplet 2 collides droplet 1 of the same volume and physical properties with velocity  $v$  and forms a new droplet with droplet 1. A constant temperature no-slip wall boundary is used for the bottom wall, and the pressure boundary condition is used for the rest of walls.

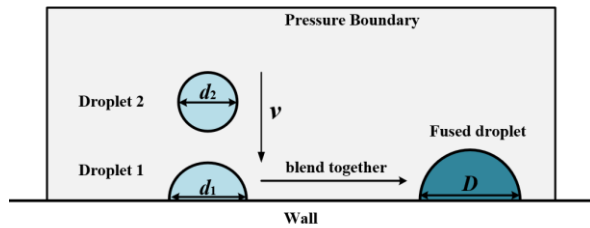


Figure 1 Schematic diagram of double droplets with low velocity positive collision

### 2.1 Mass and Momentum Transfer

The model is mainly selected for numerical simulation of laminar two-phase flow and horizontal set of multi-physics fields suitable for droplet motion. Since air is forced to flow by droplet motion in the model, the changes of velocity, pressure and temperature are small, and the density can still be viewed as a constant. Therefore, the N-S equations for incompressible fluids are chosen to model the mass and momentum transfer in air-liquid two-phase fluids.

The N-S equation is

$$\rho \left( \frac{\partial u}{\partial t} + u \cdot \nabla u \right) - \nabla \cdot \left[ \mu (\nabla u + \nabla u^T) \right] + \nabla p = F_{st} \quad (1)$$

The continuity equation is

$$\nabla \cdot u = 0 \quad (2)$$

where  $\rho$  is density;  $\mu$  is kinetic viscosity;  $u$  is velocity;  $P$  is pressure; and  $F_{st}$  is surface tension.

## 2.2 Solidification-melting model

In considering the droplet phase change, an enthalpy-porosity phase change model is used to simulate the solidification-melting phase change process inside the droplet [16-17], and the energy equation for the computational solution is

$$\frac{\partial}{\partial t}(\rho H) + \nabla(\rho v H) = \nabla(k \nabla T) \quad (3)$$

where  $\rho$  is the density,  $H$  is the enthalpy,  $v$  is the collide velocity, and  $k$  is the thermal diffusion coefficients. After considering the phase change, the enthalpy in the energy equation is the sum of sensible heat and latent heat,  $H = c_p T + \Delta H$ . Where the latent heat part is related to the latent heat of solidification/melt phase change of water as

$$\Delta H = L_f \gamma \quad (4)$$

where  $c_p$  is the specific heat capacity and  $L_f$  is the latent heat. The enthalpy-porosity phase change model treats the ice-water mixing region as a porous structure, and the porosity is the volume fraction  $\gamma$  of the liquid phase, which takes the value interval [0,1] and is related to the temperature as

$$\gamma = \begin{cases} 1 & T \geq T_{\text{liquid}} \\ \frac{T - T_{\text{solid}}}{T_{\text{liquid}} - T_{\text{solid}}} & T_{\text{solid}} \leq T < T_{\text{liquid}} \\ 0 & T < T_{\text{solid}} \end{cases} \quad (5)$$

where  $T$  is the temperature,  $T_{\text{solid}}$  is the freezing temperature, and  $T_{\text{liquid}}$  is the melting temperature.

## 2.3 Calculation method

The numerical model is calculated using a 2D model, which can more clearly capture the movement changes of the gas-liquid free interface and reduce computational complexity. For meshing, a grid of approximately 78,000 square triangles is used to mesh a two-dimensional area of 20×20 mm. The computational work gases are set to air and water, and the set droplet physical properties (see Table 1), as well as parameters such as collide velocity  $v$ , wall temperature  $T_w$ , and contact angle  $\theta$  are set. The pressure and velocity fields are calculated using the PARDISO solver, and the temperature field is calculated using the MUMPS solver. Then the cloud map of liquid phase volume fraction distribution is established to visualize and monitor the impact process. Finally, the convergence calculation is carried out when the residual is less than  $10^{-6}$ .

Table 1 Physical properties of liquid droplet

Viscosity $\mu$	0.001 kg/(m·s)
Density $\rho$	1000 kg/m <sup>3</sup>
Surface tension coefficients $\sigma$	0.0728 N/m
Specific heat $c_p$	4182 J/kg·K
Thermal conductivity $\lambda$	0.6 W/m·K
Melting latent heat $L_f$	333000 J/kg
Droplet temperature $T_{\text{water}}$	10 °C
Phase change temperature $T_{\text{ice}}$	0 °C

### 3. Validation of the numerical model

In order to verify the accuracy of the model, the experimental system is constructed. As shown in Figure 2, it mainly consists of a droplet generation system, an experimental platform, a high-precision image acquisition system, a data acquisition system and a low temperature cooling circulatory system.

The droplet generation system is mainly composed of a microfluidic syringe pump, a piezoelectric actuator composed of multilayer piezoelectric sheets and a nozzle. By adjusting the voltage and the displacement of the piezoelectric sheet, the force of the droplet can be changed to obtain droplets with different velocities, and the size of the nozzle can be changed to obtain droplets with different diameters. The experimental platform consists of a copper wall surface, a constant temperature environmental chamber and a thermoelectric cooling system. The image acquisition system consists of two high-precision high-velocity cameras and a calculator. The data acquisition system consists of a data collector for reading data, a surface measuring instrument for observing the wall contact angle, and a temperature thermocouple for measuring the wall temperature. The dynamic process of droplet collision is recorded by the high-velocity video camera (the shooting speed is 1200 fps, and the image resolution is  $1024 \times 768$  pixels), and the captured images are processed by the software to obtain the droplet height at different moments. The low temperature cooling circulatory system consists of a low-temperature constant temperature cooling circulating water tank and circulating water pipes, whose main function is to be responsible for the heat exchange on the wall surface.

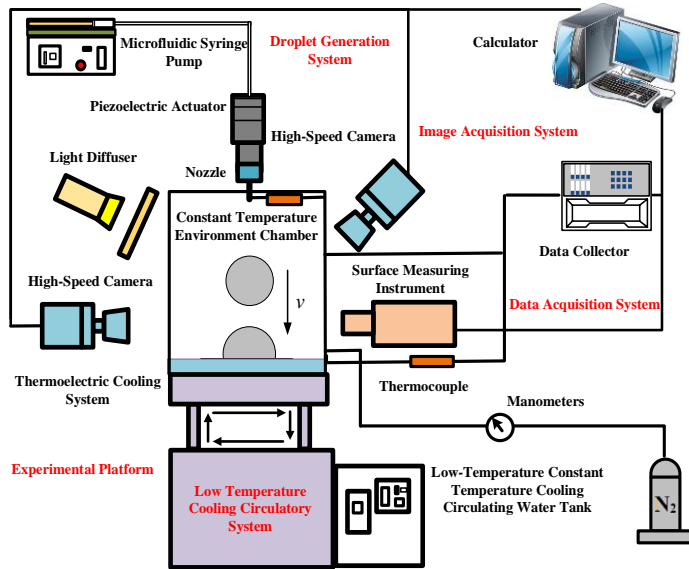


Figure 2 Schematic diagram of the experimental system

Figure 3 shows the comparison of the dynamic process of double droplets positive collision under experimental observation and numerical simulation method ( $d_2=4$  mm,  $\theta=70^\circ$ ,  $v=0.2$  m/s,  $T_w=5$  °C). From the figure, it can be seen that the droplet motion patterns of experimental observation and numerical simulation are consistent for the same time.

(i)  $t=-69$  ms (ii)  $t=-45$  ms (iii)  $t=0$  ms (iv)  $t=21$  ms (v)  $t=52$  ms (vi)  $t=168$  ms (vii)  $t=900$  ms

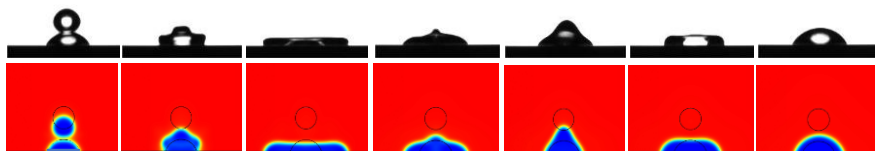


Figure 3 Comparison of the dynamic process of double droplets positive collision between

experimental observation and numerical simulation

Figure 4 shows the quantitative comparison curves of the real vibration height of the fused droplet from experimental observation and numerical simulation. As shown in the figure, the droplets height with time changes consistently, and the errors of vibration time and peak value are 10.6% and 5.36% respectively, which verifies the reliability of the numerical model.

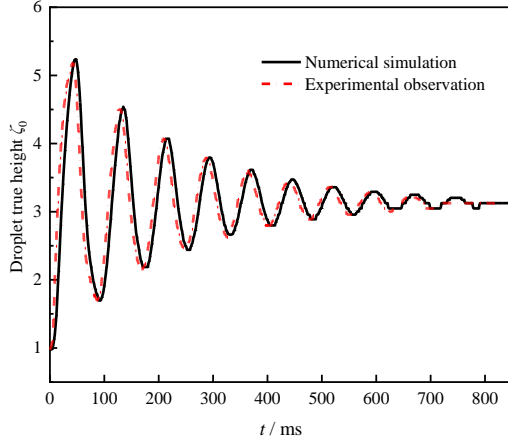


Figure 4 Comparison curves of real vibration height of droplets

## 4. Calculation results and analysis

### 4.1. Research of spreading characteristics

Figure 5 shows the phase diagram of the dynamic process of spreading of the same volume of double droplets positive collision under different conditions. As shown in Figure 5 (a), the moment when droplet 2 touches droplet 1 (Figure (a) i), which is the beginning of the collision process and the fusion process. During the collide process (Figures (a) ii-vi), the bottom of droplet 2 gradually squeezes the top of droplet 1, causing the top waters of droplet 1 to stretch to the sides and gradually fall down. This state continues until the end of the collide process (Figure (a) vii). At the end of the collide process, droplet 1 and droplet 2 are completely fused into a new droplet and the fused new droplet reaches the maximum spreading. In Figure 5 (a) compared to (b), droplet 2 has a larger diameter, consumes more time to reach the maximum spreading of the fused droplet, and has a larger spreading area. Figure 5 (a) compared with (c), droplet 2 has a larger collide velocity, and the fused droplet consumes less time to reach maximum spreading and has a larger spreading area. Figure 5 (a) Compared with (d), the wall contact angle is larger, the fused droplet consumes less time to reach the maximum spreading, and the spreading area is smaller.

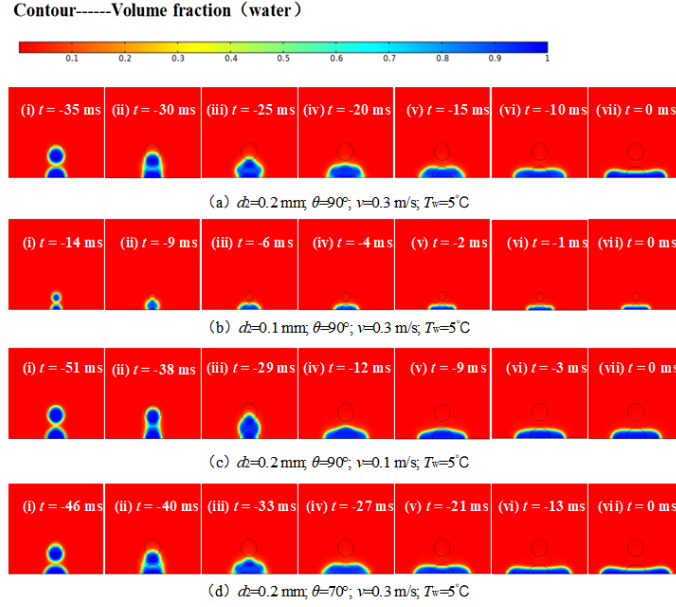
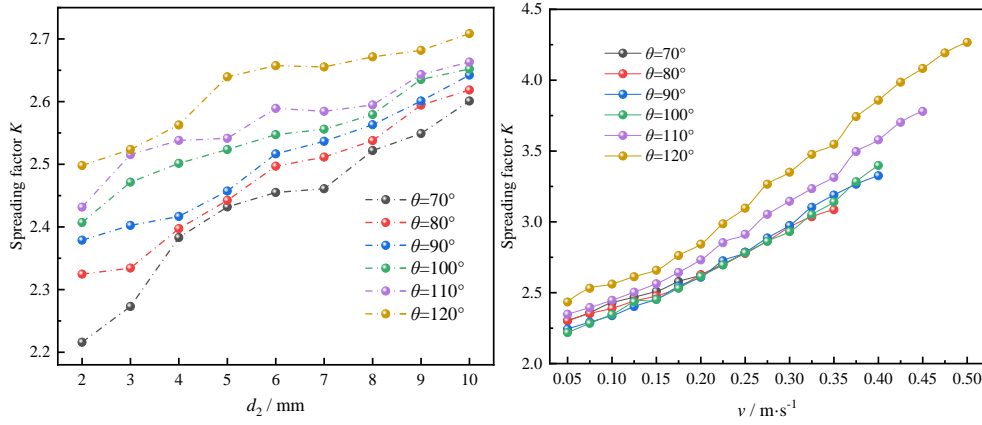


Figure 5 The evolution of double droplets positive collision spreading at various time points

To investigate the extent to which the double droplets spreads on the wall, the spreading factor  $K$  is introduced here,  $K = D_{\max} / d_1$ . Figure 6 (a) shows the comparison curves of spreading factors corresponding to droplet 2 diameters under different wall contact angle conditions ( $T_w = 5^\circ \text{C}$ ,  $v = 0.1 \text{ m/s}$ ). It can be seen from the figure that the spreading factors of fused droplet gradually increases with the increase of droplet 2 diameter. This is due to the fact that the larger the droplet 2 diameter is, the greater the inertial force it has when falling under the condition of uniform collide velocity. The lateral force that is transformed into the squeezing droplet 1 and the force of its own spreading during the collide process is also greater, promoting the spreading of the fused droplet. In addition, by increasing the wall contact angle, the spreading factor also increases. This is due to the fact that on a wall with a smaller contact angle, the better the wall wettability, the larger the spreading area presented by droplet 1, which makes droplet 2 suffer more viscous resistance from droplet 1 in the lateral spreading process and the spreading degree is reduced.

Figure 6 (b) shows the comparison curves of spreading factors corresponding to the collide velocity under different wall contact angle conditions ( $d_2 = 4 \text{ mm}$ ,  $T_w = 0^\circ \text{C}$ ). It can be seen from the figure that the spreading factors of fused droplet gradually increases as the collide velocity of droplet 2 increases. This is due to the fact that under the condition of uniform droplet 2 diameter, the larger the collide velocity is, the larger the inertial force is, which will promote the spreading of the fused droplet. Under the condition of increasing collide velocity, the values of spreading factor are very close in the range of  $70^\circ \sim 100^\circ$  of contact angle, and there is no change pattern of spreading factor. However, the spreading factor gradually increases with the increase of contact angle in the range of  $100^\circ \sim 120^\circ$ . And the larger the contact angle is, the larger the velocity required for the fused droplet to break.



(a) Variation of spreading factors vs.  $d_2$  (b) Variation of spreading factors vs.  $v$   
Figure 6 Comparison curves at different wall contact angles

#### 4.2. Research of vibration characteristics

Figure 7 shows the phase diagram of the vibration processes of the fused droplet with different wall temperatures ( $d_2=2$  mm,  $v=0.2$  m/s,  $\theta=90^\circ$ ,  $T_w = -20$  and  $0$  °C). As shown in Figure 7 (a), after the fused droplet reaches the maximum spreading, it is squeezed by the surface tension on both sides and the heat transfer from the bottom wall, the bottom of the droplet freezes and the top of the droplet protrudes upward, and the "bullet head" shape drives the reciprocal rebound vibration on both sides. Until the kinetic energy introduced by droplet 2 is dissipated through viscosity and comes to rest at the wall. In Figure 7 (a), compared with (b), the wall temperature is lower, the amount of ice at the bottom of the fused droplet are higher, and the time consumed for the droplet to come to rest is shorter.

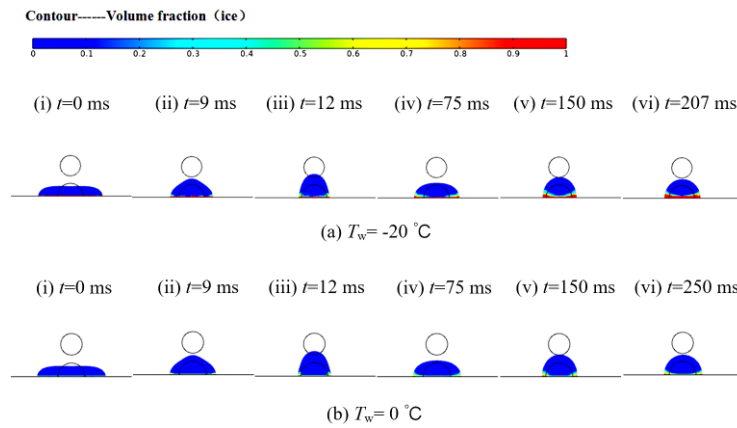


Figure 7 The vibrational processes of fused droplets at different wall temperatures

To further describe the vibration process, a theoretical model of a single-degree-of-freedom damped vibration system is used to analyze the droplet vibration behavior, and the droplet center height variation can be expressed by the damped vibration equation

$$m\ddot{\zeta}_0 + c\dot{\zeta}_0 + k\zeta_0 = 0 \quad (6)$$

where  $\ddot{\zeta}_0$ ,  $\dot{\zeta}_0$  are the first and second order derivatives of the true height  $\zeta_0$  of the droplet, respectively. the damping coefficients  $c=2m\varepsilon$ . The general solution is obtained by calculating the second order linear chi-square differential equation

$$\zeta_0 = \zeta_{eq} + [A\cos(wt) + B\sin(wt)]e^{-\varepsilon_0 t} \quad (7)$$

$$\zeta_0 = \zeta_{eq} + C_0 e^{-\varepsilon_0 t} \quad (8)$$

where  $\zeta_{eq}$  is the droplet rest height.  $C_0$  and  $\varepsilon_0$  are the fitting coefficients.  $w$  is the angular frequency. A, B are the two coefficients determined by the initial conditions.  $t$  is the vibration time.

In order to more accurately express the numerical variation of the droplet's vibration height, a dimensionless parameter is defined here - the ratio of the droplet's vibration height  $\zeta$ , the droplet's true height  $\zeta_0$  to its resting height  $\zeta_{eq}$ . Substituted into equation (8) as

$$\zeta = 1 + Ce^{-\varepsilon t} \quad (9)$$

where  $C$  and  $\varepsilon$  are the fitting coefficients, and  $t$  is the vibration time, ms (all the vibrations of a single cycle of the droplet are in milliseconds, so milliseconds are used for the calculation).

During the rebound vibration of fused droplet, the top region is subjected to heat transfer from the bottom while at the same time heat exchange with the adjacent waters, which can reduce the heat transfer efficiency. If the vibration damping coefficient of the droplet is small, the greater the amplitude and vibration duration during the vibration. The heat exchange time and heat exchange between the top of the droplet and the adjacent waters will increase, which reduces the heat transfer efficiency and prolongs the time of complete phase change of the droplet.

Figure 8 shows the variation curves and fitted the curves of the vibration height of the fused droplet at different collide velocities ( $d_2=4$  mm,  $T_w=15$  °C,  $\theta=80$  °). As can be seen from the figure, increasing the collide velocity, the amplitude and vibration time of the fused droplet gradually increase. This is due to the fact that the larger the velocity of droplet 2 is, the more kinetic energy is introduced into the impingement system to promote droplet spreading under the same droplet diameter and dynamic viscosity. And with more energy into the rebound vibration, making the amplitude larger and the vibration time longer.

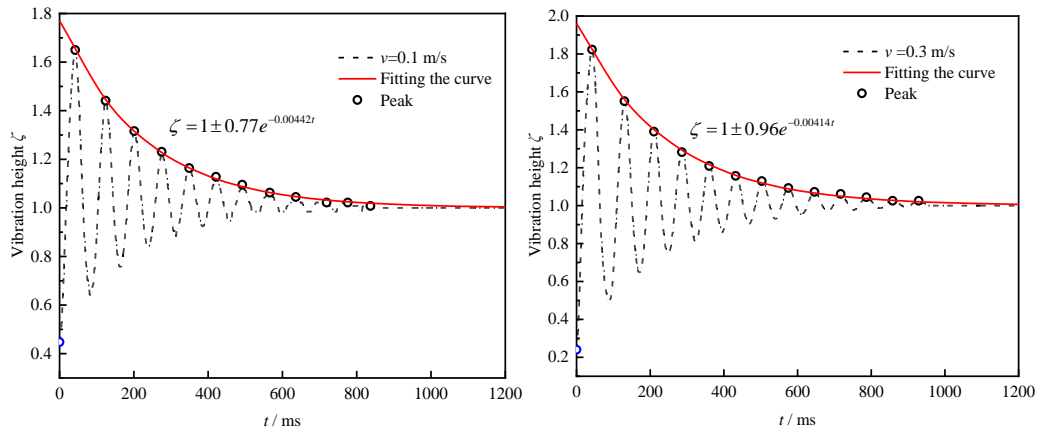
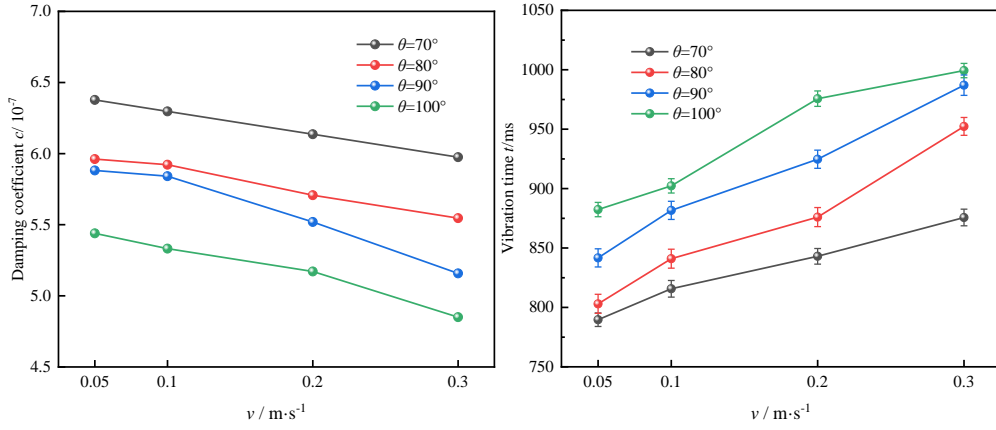


Figure 8 Curves and fitted the curves of fused droplet vibration height variation

Figure 9 (a) and (b) shows the comparison curves of the vibration damping coefficients and vibration time of fused droplet with the change of collide velocity under different wall contact angles. It can be seen that the vibration damping coefficients gradually decreases and the vibration time of droplets gradually increases with the increase of collide velocity and wall contact angle.





(a) Variation of damping coefficients vs.  $\nu$  (b) Variation of vibration time vs.  $\nu$   
Figure 9. Comparison curves of fused droplet at different wall contact angles

Figure 10 shows the variation curves and fitted the curves of the vibration height of the fused droplet at different wall temperatures ( $\nu=0.2 \text{ m/s}$ ,  $\theta=90^\circ$ ,  $d_2=4 \text{ mm}$ ). As can be seen from the figure, the droplets vibration time gradually decreases as the wall temperature decreases, but the maximum amplitude is very close. This is due to the low wall temperature, which causes the viscosity coefficients of the droplets to increase. If the wall temperature reaches the temperature that drives the phase change at the bottom of the droplets, the droplets undergo a phase change that will inhibit the fluid flow.

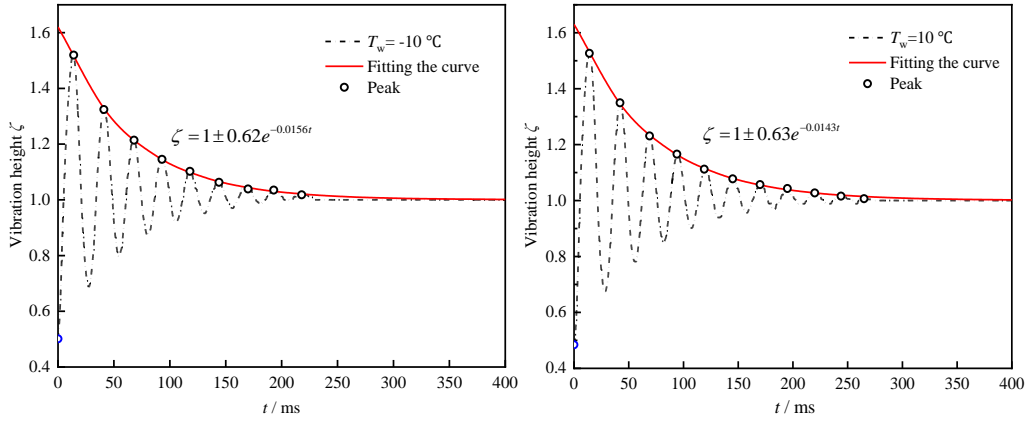
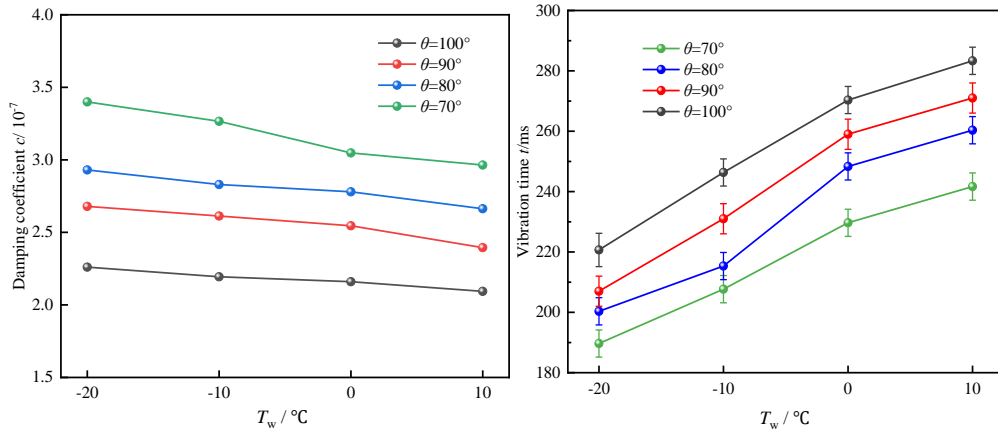


Figure 10 Curves and fitted the curves of fused droplet vibration height variation

Figure 11 (a) and (b) show the comparison curves of the damping coefficients of fused droplet vibration with the change of wall temperature at different contact angles. From the figures, it can be seen that the vibration damping coefficients gradually decreases and the vibration time gradually increases with the increase of the wall temperature and contact angle.



(a) Variation of damping coefficients vs.  $T_w$  (b) Variation of vibration time vs.  $T_w$   
Figure 11. Comparison curves of fused droplet at different contact angles

### 4.3. Research of rebound fracture characteristics

Figure 12 shows the rebound fracture pressure of the double droplets after positive collision at different time points ( $d_2=4$  mm,  $\theta=90^\circ$ ,  $T_w=15$   $^\circ\text{C}$ , and  $v=0.45$  m/s). As shown in the figure, the convex droplet 2 bottom and droplet 1 top start to spread to both sides after positive collision (Figures. i-ii). The pressure at the bottom of droplet 2 and the top of droplet 1 is maximum on both sides, and this state continues until the fused droplet reaches the moment of maximum spreading (Figure iii). Then the fused droplet is subjected to the counteraction of surface tension and starts to enter the rebound vibration period (Figure iv). During the rebound period, the waters on both sides and the maximum pressure gradually converge toward the center (Figures v-vi). The waters on both sides continuously stretch the central waters, making the central waters gradually lower and the waters on both sides gradually higher. If the collide velocity of droplet 2 increases, the inertial force when falling will increase, making the fused droplet spread more and spread at a lower height, and the pull of rebound occurs on both sides by surface tension. In the rebound period, if the height of the central water of the fused droplet is lower as well as the pull force of the rebound of the water on both sides is greater, it is more likely to lead to the rebound fracture of the central water (Figure vii).

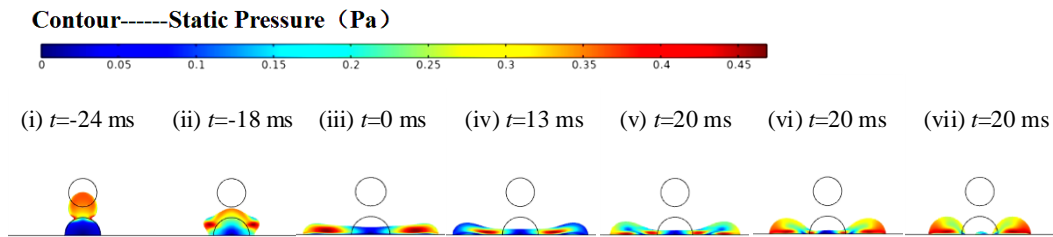


Figure 12 Rebound fracture pressure of the double droplets under positive collision at different time points

Figure 13 shows the critical collide velocity comparison curves for rebound fracture at different wall contact angles. It can be seen that the critical collide velocity required for rebound fracture of fused droplet decreases as the droplet 2 diameter increases. This is due to the fact that the larger the diameter (inertial force) of droplet 2, the greater the pulling force on both sides of the rebound, making the central waters gradually become lower and more prone to rebound fracture. As the wall contact angle decreases, the critical collide velocity required for the fused droplet to rebound and fracture also decreases. This is due to the fact that the larger the wall contact angle, the less wetting of the wall

surface. The height of the fused droplet spreading on the wall to the maximum moment is higher, and the central water height of the fused droplet at rebound is higher and less prone to fracture. Therefore a greater collide velocity is required for rebound fracture to occur.

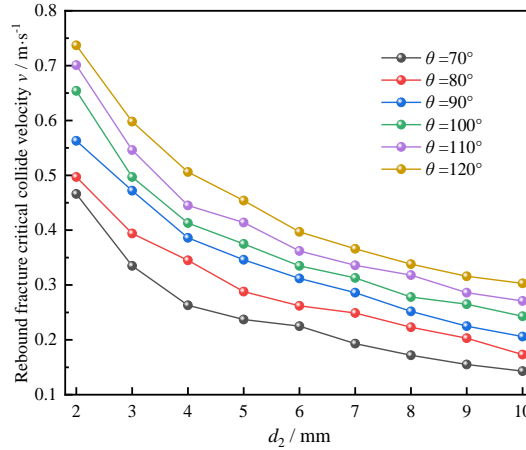


Figure 13 Comparison curves of critical collide velocity for rebound fracture

#### 4.4. Research of spreading fracture characteristics

Figure 14 shows the spreading fracture pressure of the double droplets after positive collision at different moments ( $d_2=4$  mm,  $\theta=90^\circ$ ,  $T_w=15$  °C,  $v=0.8$  m/s). As shown in the figure, based on the occurrence of rebound fracture, continuing to increase the collide velocity will accelerate the collide process of droplet 2 (Figures i-v) and fuse to produce the spreading fracture phenomenon. This is due to the increase in the collide velocity (inertial force) of droplet 2, which will increase the lateral force of squeezing droplet 1 and the pulling force of spreading itself to both sides. During the spreading period, the fused droplet is continuously subjected to excessive tension on both sides, resulting in spreading fracture of the fused droplet (Figure vi).

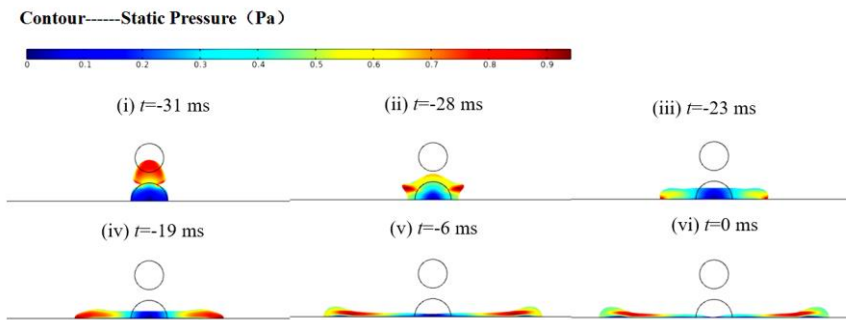


Figure 14 Spreading fracture pressure of the double droplets under positive collision at different time points

Figure 15 shows the critical collide velocity comparison curves for spreading fracture at different wall contact angles. It can be seen that the critical collide velocity required for spreading fracture of the fused droplet decreases as the droplet 2 diameter increases. This is because the larger the diameter of droplet 2 (inertial force), the greater the lateral force of squeezing droplet 1 and its own spreading tension to both sides during the collide process, the easier it is to tear the central waters and occur the spreading fracture phenomenon. As the wall contact angle decreases, the critical collide velocity required for the fused droplet to spread and fracture also decreases. This is due to the fact that the larger the wall contact angle, the less wetting of the wall surface. The fused droplet spread less on the wall, have a higher spread height and are less likely to tear the central waters. Therefore, a greater

collide velocity (lateral force) is required to stretch the central waters to both sides in order for the spreading fracture to occur.

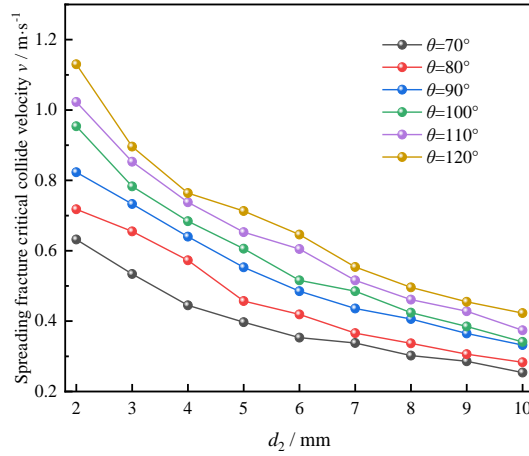


Figure 15 Comparison curves of critical collide velocity for spreading fracture

## 5. Conclusion

In this paper, the kinetic properties of double droplets under positive collision in low velocity were studied by numerical simulation compared with the results of the experiment. The main conclusions obtained are as follows:

(1) In the spreading process, the spreading factor of fused droplet gradually increases with the increase of droplet diameter, collide velocity and contact angle of the wall. However, the spreading factor gradually increases with the increase of contact angle when the contact angle is in the range of  $100^\circ \sim 120^\circ$  under the condition of increasing velocity. In contrast, the spreading factors at different collide velocities are very similar in the contact angle range of  $70^\circ \sim 100^\circ$ , and there is no obvious pattern of change.

(2) In the vibration process, the theoretical model of single-degree-of-freedom damped vibration system is used to analyze the vibration behavior of the fused droplet. With the decrease of collide velocity and wall contact angle, the vibration damping coefficients of the fused droplet gradually increases, and the vibration time and vibration amplitude decrease.

(3) In the vibration process, the influence of low wall temperature will lead to an increase in the viscosity coefficients of the droplet. If the cold wall surface drives the droplet to undergo phase change, it will inhibit the fluid flow, leading to an increase in the damping coefficient and a decrease in vibration time.

(4) Rebound fracture and spreading fracture may occur after the fusion of double droplets under positive collision. With the increase of droplet diameter and the decrease of wall contact angle, the critical collide velocity required for the fracture of fused droplet gradually decreases.

## Acknowledgments

This research was funded by the National Natural Science Foundation of China, grant number 51905406, the Basic Research Plan of Natural Science in Shaanxi Province, grant number 2021JQ-650 and Scientific Research Program Funded by Shaanxi Provincial Education Department, grant number 19JK0412.

Nomenclature			
$K$	spreading factor	Greek symbols	
$v$	collide velocity(m/s)	$\theta$	Wall contact angle (°)
$T_w$	wall temperature (°C)	$\zeta$	vibration height
$d_2$	droplet 2 diameter(mm)	Subscripts and superscripts	
$t$	vibration time(ms)	w	wall
$c$	damping coefficient	2	droplet 2

## REFERENCE

- [1] Wang, X., Xu, B., Guo, S., Zhao, Y., *et al.*, Droplet Impacting Dynamics: Recent Progress and Future Aspects, *Advances in Colloid and Interface Science*, 317(2023), pp. 102919 DOI No. 10.1016/J.CIS.2023.102919
- [2] Gao, S.R., Jin, J.X., Wei, B.J., *et al.*, Dynamic Behaviors of Two Droplets Impacting an Inclined Super hydrophobic Substrate, *Colloids and Surfaces A: Physicochemical and Engineering Aspects*, 623(2021), pp. 126725 DOI No. 10.1016/J.COLSURFA.2021.126725
- [3] Wang, Y.B., Wang, Y.F., Gao, S.R., *et al.*, A Universal Model for the Maximum Spreading Factor of Impacting Nanodroplets: From Hydrophilic To hydrophobic Substrates, *Langmuir: the ACS journal of surfaces and colloids*, 36(2020), pp. 9306-9316 DOI No. 10.1021/acs.langmuir.0c01879
- [4] Lamini, O., Wu, R., Zhao, C.Y., *et al.*, Experimental Study on the Effect of the Liquid/Surface Thermal Properties on Droplet Impact, *Thermal Science*, 25(2021), 1, pp. 705-716 DOI No. 10.2298/tsci1909051421
- [5] Wang, X., Lin, D.J., Wang, Y.B., *et al.*, Rebound Dynamics of Two Droplets Simultaneously Impacting a Flat Superhydrophobic Surface, *Aiche Journal*, 66 (2020), pp. 16647 DOI No. 10.1002/aic.16647. DOI No. 10.1002/aic.16647
- [6] Wang, Y.F., Wang, Y.B., Xie, F.F., *et al.*, Spreading and Retraction Kinetics for Impact of Nanodroplets on Hydrophobic Surfaces, *Physics of Fluids*, 32 (2020), pp. 092005 DOI No. 10.1063/5.0020675
- [7] Ravichandar, K., Olsen, M.G., Dennis, V.R., Turbulent Droplet Breakage Probability: Analysis of Fitting Parameters for Two Commonly Used Models, *Chemical Engineering Science*, 266(2023), pp. 118311 DOI No. 10.1016/J.CES.2022.118311
- [8] Fujimoto, H., Tong, A.Y., Takuda, H., Interaction Phenomena of Two Water Droplets Successively Impacting onto a Solid Surface, *International Journal of Thermal Sciences*, 47 (2008), pp. 229-236 DOI No. 10.1016/j.ijthermalsci.2007.02.006
- [9] Fujimoto, H., Yoshimoto, S., Takahashi, K., *et al.*, Deformation Behavior of Two Droplets Successively Impinging Obliquely on Hot Solid Surface, *Experimental Thermal and Fluid Science*, 81(2017), pp. 136-146 DOI No. 10.1016/j.expthermflusci.2016.10.009
- [10] Yuvaraj, R., Senthil, K., Study of Droplet Dynamics and Condensation Heat Transfer on Superhydrophobic Copper Surface, *Thermal Science*, 24(2021), 1, pp. 653-664 DOI No. 10.2298/tsci190126089y

- [11] Lin, S.J., Zhao, B.Y., Zou, S., *et al.*, Impact of Viscous Droplets on Different Wettable Surfaces: Impact Phenomena, The Maximum Spreading Factor, Spreading Time and Post-impact Oscillation, *Journal of Colloid and Interface Science*, 516(2018), pp. 8697 DOI No. 10.1016/j.jcis.2017.12.086
- [12] Manglik, R.M., Jog, M.A., Gande, S.K., *et al.*, Damped Harmonic System Modeling of Post-Impact Drop-spread Dynamics on a Hydrophobic Surface, *Physics of Fluids*, 25(2013), 8, pp. 082112 DOI No. 10.1063/1.4819243
- [13] Ravi, V., Jog, M.A., Manglik, R.M., Effects of Pseudoplasticity on Spread and Recoil Dynamics of Aqueous Polymeric Solution Droplets on Solid Surfaces, *Interfacial Phenomena and Heat Transfer*, 1(2013), 3, pp. 273-287 DOI No. 10.1615/INTERFACPHENOMHEATTRANSFER.2013010246
- [14] Fedorchenko, A.I., Effect of Capillary Perturbations on the Dynamics of a Droplet Spreading over a Surface, *Russian Journal of Engineering Thermophysics*, 10(2000), 1, pp. 1-11 DOI No. 10.1063/1.2038367
- [15] Sharp, J.S., Farmer, D.J., Kelly, J., Contact Angle Dependence of the Resonant Frequency of Sessile Water Droplets, *Langmuir the Acs Journal of Surfaces & Colloids*, 27(2011), 15, pp. 9367-9371 DOI No. 10.1021/la201984y
- [16] Jung S., Tiwari, M.K., Doan, N.V., *et al.*, Mechanism of Super Cooled Droplet Freezing on Surfaces, *Nature Communications*, 3(2012), pp. 1630 DOI No. 10.1038/ncomms1630
- [17] Voller, V., Rprakash, C., A Fixed Grid Numerical Modelling Methodology for Convection-diffusion Mushy Region Phase-change Problems, *International Journal of Heat and Mass Transfer*, 30(1987), 8, pp. 1709-1719 DOI No. 10.1016/0017-9310(87)90317-6

- Paper submitted: 13 June 2023
- Paper revised: 23 September 2023
- Paper accepted: 07 October 2023